



Planar time-resolved laser-induced incandescence for pressurized premixed Jet-A combustion

Andy X. Zheng¹ · Sundar Ram Manikandan² · Samuel E. Wonfor² · Adam M. Steinberg² · Yi Chen Mazumdar¹

Received: 18 January 2023 / Accepted: 3 April 2023 / Published online: 18 April 2023
© The Author(s), under exclusive licence to Springer-Verlag GmbH Germany, part of Springer Nature 2023

Abstract

Understanding soot formation in flames burning Jet-A fuel at elevated pressures is critical for reducing emissions from aeroengine combustion. In this work, we utilize a single camera single laser shot two-dimensional (2D) time-resolved laser-induced incandescence (TiRe-LII) technique to acquire soot incandescence decay images at 10 MHz in premixed prevaporized Jet-A/air flames at 1, 2.4, and 3.8 bar. By using a TiRe-LII model, the incandescence decay signals are mapped to primary particle size estimates. Then, model estimates are compared with *in-situ* soot samples, which are collected using a custom designed thermophoretic sampling system and analyzed with transmission electron microscopy. Results show small soot particle diameters between 13 and 16 nm and large aggregates with approximately 200 particles on average. A good match is obtained between the TiRe-LII and extracted soot sample data, where estimates are within 2 nm for all test conditions. This work illustrates how a single camera LII measurement technique can be implemented with a TiRe-LII model to obtain instantaneous 2D estimates of soot primary particle sizes in pressurized systems. By using this imaging TiRe-LII technique, soot formation in more complex and realistic gas turbine combustors can potentially be investigated.

1 Introduction

Practically relevant combustion systems often result in the emission of non-volatile particulate matter (nvPM), which is composed primarily of soot. Soot in the atmosphere drives climate change through radiative forcing [1, 2] and has several adverse health effects [3, 4] associated with diagnoses of respiratory symptoms, ischemic heart disease, and

cerebrovascular disease [5]. Furthermore, soot production leads to reduced engine efficiency, increased radiative heat losses, and decreased combustor durability due to liner defacement [6]. Therefore, understanding the production of flame-generated soot is essential for facilitating the design of efficient, reliable, and low emission combustors.

The formation and oxidation of soot are complex processes involving combustion chemistry, phase change, and heat transfer coupled with turbulence effects. While *in-situ* sampling has been used extensively to study soot particle sizes [7, 8], these techniques suffer from the use of intrusive mechanical probes, soot modification after sampling, and complexities with probe deployment at high pressures and temperatures. Laser-based optical diagnostics, on the other hand, can be applied non-intrusively in the middle of the flame to estimate soot properties. Laser-induced incandescence (LII), in particular, is a diagnostic that can be used to measure volume fraction and primary particle size for soot [9, 10], as well as non-soot particulates [11].

In order to obtain spatially resolved measurements, two-dimensional (2D) imaging techniques can be used. Recently, a simple single camera and single laser shot 2D time-resolved laser-induced incandescence (2D TiRe-LII) method was developed [12] for spatially and temporally resolved measurements. In this method, soot particles are

✉ Andy X. Zheng
azheng36@gatech.edu

Sundar Ram Manikandan
smanikandan7@gatech.edu

Samuel E. Wonfor
swonfor@gatech.edu

Adam M. Steinberg
adam.steinberg@gatech.edu

Yi Chen Mazumdar
ellen.mazumdar@gatech.edu

¹ George W. Woodruff School of Mechanical Engineering, Georgia Institute of Technology, 801 Ferst Dr NW, Atlanta, GA 30318, USA

² Daniel Guggenheim School of Aerospace Engineering, Georgia Institute of Technology, 270 Ferst Dr NW, Atlanta, GA 30313, USA

heated with a laser pulse and the incandescence decay time is acquired using a MHz-rate camera. While the data acquisition method is straightforward, converting the acquired optical signals to primary soot particle sizes can be complex due to unknown aggregate sizes and shielding effects [13]. Additionally, high-pressure environments can reduce decay timescales and soot restructuring from the presence of water and polycyclic aromatic hydrocarbons (PAHs) can alter optical properties [14]. Thus, practical application of 2D TiRe-LII requires studies with relevant fuels and at relevant conditions to further develop the diagnostic.

Most LII models in the literature today are studied with experimental data from ethylene diffusion flames at atmospheric pressure [15, 16, 17, 18]. In many of those studies, soot is directly sampled and transmission electron microscopy (TEM) measurements are used to estimate particle sizes for comparison with LII measurements and models [19, 20]. For high-pressure conditions, some studies show that incandescence signals decay faster with increasing pressure [21] and that the decay rate increases linearly with pressure [22]. Studies in high-pressure diesel combustion environments [23, 24, 25, 26], on the other hand, indicate that the morphological characteristics of soot also play an important role and emphasize that more accurately calibrated LII models are needed at elevated pressures. While LII has been used previously to estimate soot volume fractions in Jet-A fuel combustion at elevated pressures [27], there are currently no studies in the literature that estimate soot particle sizes with 2D TiRe-LII for Jet-A fuel at similar pressures. Thus, there is a need for experimental soot sampling data and 2D TiRe-LII data for Jet-A fuel at elevated pressures.

In this work, we deploy a single camera, single laser shot 2D TiRe-LII technique to investigate soot particle sizes in laminar premixed Jet-A flames at elevated pressure conditions. Each pixel in this unique 2D dataset is fit to a LII model in order to determine particle size estimates. *In-situ* physical soot samples are obtained using a custom designed thermophoretic soot sampler. The TEM data are then compared with the TiRe-LII measurements in order to determine the accuracy of the soot particle size estimates from the LII model. This work is the first in the literature to present instantaneous 2D profiles of soot particle sizes in a Jet-A flame, as illustrated in Fig. 1, and compare results with extractive soot sampling. Additionally, it is also the first to use 2D TiRe-LII for soot particle sizing in Jet-A flames at elevated pressures. By using this diagnostic, it is possible to estimate soot particle sizes in combustor environments where extractive soot sampling is infeasible. In particular, the techniques outlined in this work can potentially be used to help reduce soot emissions in high pressure lean prevaporized premixed and rich-quench-lean aeroengine combustors for supersonic transport applications [28].

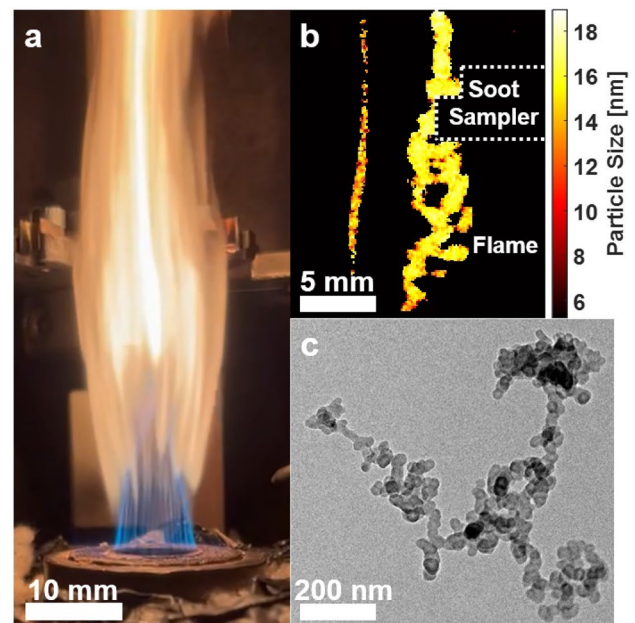


Fig. 1 a Example of a flame inside a pressure vessel where b TiRe-LII data and c extracted soot samples are collected

2 Laser-induced incandescence model

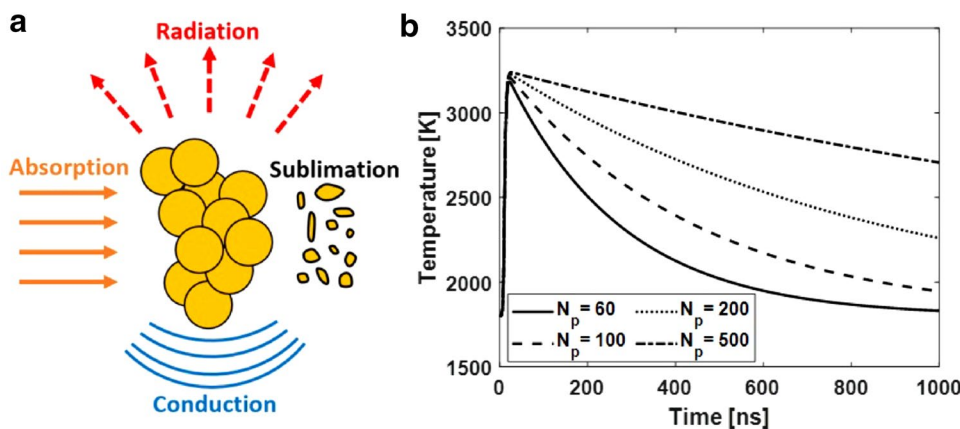
LII models typically use energy conservation equations to predict soot incandescence decay profiles. Most LII models [29, 30] account for the internal energy of the soot particles, absorption of incident laser beam energy, radiation losses, and conduction losses, as illustrated in Fig. 2a. The energy conservation equation can be expressed as,

$$\frac{dU_{Internal}}{dt} = \dot{Q}_{Absorption} - \dot{Q}_{Conduction} - \dot{Q}_{Radiation}. \quad (1)$$

For high laser fluences (above 200 mJ/cm² at a laser wavelength of 1064 nm [9, 10]), sublimation, mass loss, and other terms can also be included [31]. For particle sizing, however, it is preferable to avoid sublimation effects as sublimation reduces the particle sizes significantly after laser incidence, complicates LII modeling with mass balance equations, and produces complex decay profiles that are more difficult to accurately fit. For this work, the Liu model [32], which accounts for the shielding effect of soot aggregates, is used to determine the response of soot particles to laser heating. The expressions for internal energy, absorption, and radiation are given by,

$$\frac{dU_{Internal}}{dt} = \frac{\pi}{6} d^3 N_p \rho_s c_s \frac{dT}{dt}, \quad (2)$$

Fig. 2 **a** Modes of heat transfer commonly considered in LII models are shown. **b** The effect of aggregate size N_p is illustrated for the incandescence decay profiles of soot particles with a diameter of 30 nm. The other parameters are listed in Table 1



$$\dot{Q}_{Absorption} = \frac{\pi^2 d^3 E(m) F_0 q(t) N_p}{\lambda} \tag{3}$$

$$\dot{Q}_{Radiation} = N_p \int_0^\infty \frac{8\pi^3 c^2 h}{\lambda^6} \frac{d^3 E(m)}{\exp(hc/k_B \lambda T) - 1} d\lambda \tag{4}$$

$$= \frac{199\pi^3 d^3 (k_B T)^5 E(m) N_p}{h^4 c^3} \tag{5}$$

In Eq. (4), the Planck function is integrated over all wavelengths and the Rayleigh approximation is used for the emissivity to obtain the final relationship. In these expressions, d is the soot primary particle size, N_p is the aggregate size parameter (number of primary particles per soot aggregate), ρ_s is the density of soot, c_s is the specific heat of soot, $E(m)$ is the soot absorption function, F_0 is the laser fluence, $q(t)$ is the input laser temporal profile function, λ is the wavelength of the laser, and T is the temperature. The temperature-dependent specific heat of soot is assumed to be the same as that of graphite and values are taken from the NIST-JANAF tables [33]. The temperature-dependent density is obtained by fitting to values provided by Fried and Howard [34]. The constants h , k_B , and c are the Planck constant, Boltzmann constant, and speed of light, respectively. Since low laser fluences are typically used, sublimation and mass transfer are assumed to be negligible.

Conduction of heat from the soot particle to the surrounding gas depends heavily on the conduction regime, as determined by the Knudsen number. In the regime where the mean free path exceeds the particle size of soot, conduction is in the free-molecular regime. This can be applied to experiments that take place at low pressure conditions. However, at elevated pressure conditions, the mean free path of gas molecules typically have the same size scale as the soot particles. At these conditions, conduction occurs in the transition regime, and the Fuchs method [35, 36, 37] is utilized. This method involves

finding a limiting sphere radius [38] and temperature, where inside the limiting sphere conduction is assumed to be in the free-molecular regime, and outside the sphere conduction is assumed to be in the continuum regime. The free-molecular regime conduction equation is expressed as,

$$\dot{Q}_c = \alpha \pi R_a^2 \frac{p_g}{2} \sqrt{\frac{8k_B T_\delta}{\pi m_g}} \frac{\gamma^* + 1}{\gamma^* - 1} \left(\frac{T}{T_\delta} - 1 \right), \tag{6}$$

where p_g is the ambient pressure, m_g is the mass of one of the surrounding gas molecules, T_δ is the temperature at the limiting sphere, and α is the thermal accommodation coefficient for soot. R_a is an equivalent sphere radius calculated based on the aggregate projected area [39] given by,

$$R_a = \frac{1}{2} d \left(\frac{N_p}{f_a} \right)^{1/2 \epsilon_a}, \tag{7}$$

where f_a and ϵ_a are constants with values 1.1 and 1.08, respectively [40]. Here, γ^* is an average specific heat ratio value given by the expression,

$$\frac{1}{\gamma^* - 1} = \frac{1}{T - T_\delta} \int_{T_\delta}^T \frac{1}{\gamma - 1} dT. \tag{8}$$

The number of primary particles per aggregate, N_p , is related to the radius of gyration R_g and primary particle size [41], and is given by $N_p = k_f (2R_g/d)^{D_f}$ where D_f and k_f are fractal parameters with values of 1.78 and 1.5, respectively [40]. The aggregate size can be determined from this relation, however, there is significant uncertainty in the value of k_f , as experimentally determined values often differ from numerical predictions [42]. For this study, the average aggregate size N_p was determined from direct analysis of TEM images, along with Eq. (7).

The expression for continuum regime conduction, which is assumed to be outside the limiting sphere, is given as,

$$\dot{Q}_c = 4\pi(\delta + R_a) \int_{T_g}^{T_\delta} k_g dT, \quad (9)$$

where δ is the limiting sphere boundary layer thickness used in the Fuchs method, and k_g is the thermal conductivity of the ambient gas. The temperature-dependent function for thermal conductivity from Liu et al. [43] is used for this study. The relationship between limiting sphere radius, $R_a + \delta$, and the equivalent sphere radius, R_a , is given by [35, 38],

$$\frac{\delta + R_a}{R_a} = \frac{R_a^2}{\lambda_\delta^2} \left(\frac{1}{5} \Lambda_1^5 - \frac{1}{3} \Lambda_2 \Lambda_1^3 + \frac{2}{15} \Lambda_2^5 \right). \quad (10)$$

Here, Λ_1 and Λ_2 are given by,

$$\Lambda_1 = 1 + \frac{\lambda_\delta}{R_a}, \quad (11)$$

$$\Lambda_2 = 1 + \left(\frac{\lambda_\delta}{R_a} \right)^2. \quad (12)$$

The expression for mean free path is then given as [44],

$$\lambda_g = \frac{k_g(T_g)}{fp_g} (\gamma - 1) \sqrt{\frac{\pi m_g T_g}{2k_B}}. \quad (13)$$

Lastly, the relation between the mean free path in the surrounding gas and limiting sphere is given by,

$$\lambda_\delta = \frac{k_g(T_\delta)}{k_g(T_g)} \sqrt{\frac{T_\delta}{T_g}} \lambda_g. \quad (14)$$

To find the boundary layer thickness and temperature, the conduction equations and their associated sub equations must be solved iteratively. The conduction rate is then calculated using Eqs. (6) or (9). Finally, the simulated response of a soot particle to laser heating is solved using Eq. (1) to determine the particle temperature decay over time, as illustrated in Fig. 2b. Since LII measures soot emission, the soot temperature profiles can then be converted to emission profiles at different wavelengths by assuming grey body emission, applying Planck's law, and using the emissivity coefficients for soot.

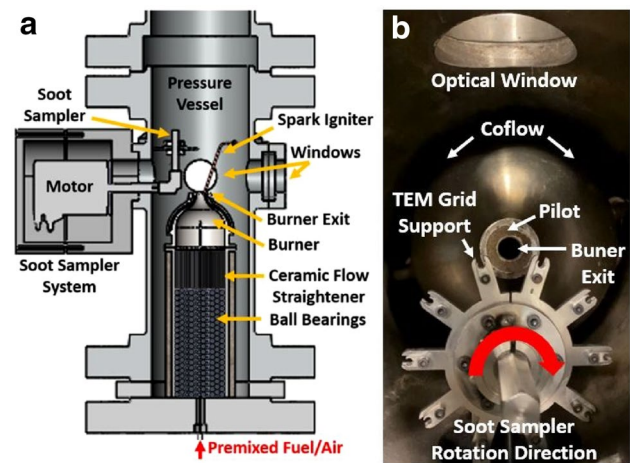


Fig. 3 **a** A schematic of the burner and pressure vessel is shown. **b** A top view of the soot sampler within the pressure vessel shows the relative location of the sampler with respect to the burner exit

3 Experimental methodology

3.1 Pressurized jet-A combustor

In this work, experiments are conducted on the laminar flame burner (LFB) [45], depicted in Fig. 3a. Here, the pressure in the vessel is controlled using a custom designed high-temperature back pressure regulator (Equilibar OEM GSDH/HT series) that can operate up to a mass flow rate, temperature, and pressure of 15 g/s, 800 K, and 12 bar, respectively. The main chamber is equipped with three ports used to accommodate windows for the incident laser beam and image acquisition as well as a chamber extension for the soot sampling system.

To meter the flow of gases and liquids, accurately calibrated critical orifices and rotameters are used. A commercial evaporator (Bronkhorst Controlled Evaporator Mixer Type W-303A-222-K) atomizes Jet-A fuel with the help of heated air in order to produce a homogeneous gaseous fuel-air mixture. To ensure good mixing and avoid fuel condensation, the piping for the premixture is heated and insulated. Fuel preheat temperatures are controlled to 475 K at the burner exit using a 600 W and 5 A Briskheat precision controller (SDXKA-Digital PID controller). Temperature feedback is obtained using a thermocouple carefully positioned near the burner exit.

Inside the pressure vessel, the premixed and prevaporized Jet-A fuel and air mixture is introduced at flowrates of 100, 200, and 350 mg/s for the 1, 2.4, and 3.8 bar test cases, respectively. The fuel and air premixture is introduced from a bottom port into a chamber filled with steel bearing balls used to ensure uniform temperature distribution, enhanced mixing, as well as serve as a secondary flashback arrester. The mixture passes through a ceramic flow straightener,

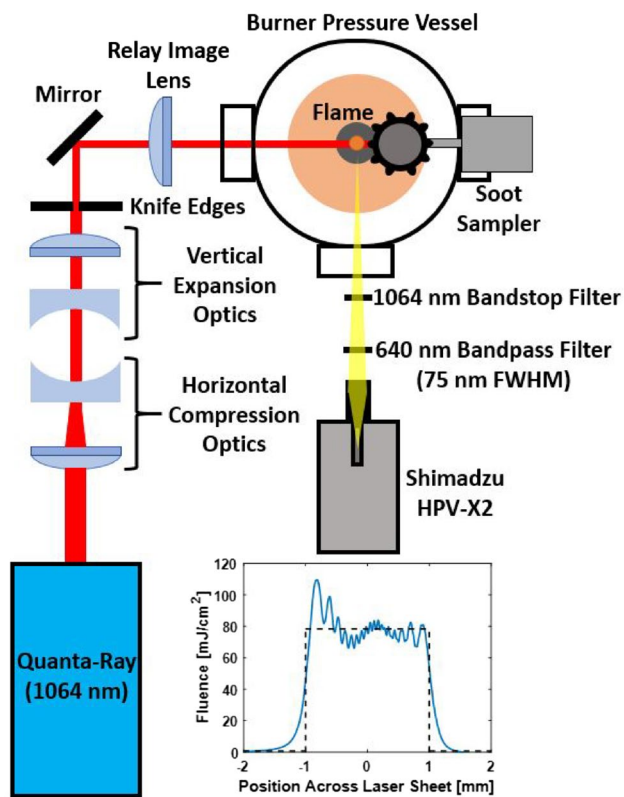


Fig. 4 Schematic of the TiRe-LII optical layout, camera, and filters is illustrated. An example of the laser profile and a tophat fit is shown at the bottom right

which also serves as a primary flashback arrester. The burner exit (diameter of $D = 9$ mm) is surrounded by nitrogen co-flow and the flame is stabilized using a stoichiometric methane-air pilot flame in a configuration that is coannular with the main nozzle. The pilot methane and air mixture flowrate was 50, 100, and 170 mg/s for the 0, 2.4, and 3.8 bar test cases. The pilot flame is ignited using a spark ignition system (10 kV and 22 mA), which in turn ignites the main flame. In this study, experiments are conducted with fuel-air ratios (FAR) of 0.16, 0.26, and 0.16 at pressures of 1 bar, 2.4 bar, and 3.8 bar, respectively. The 2.4 bar test case has a different fuel-air ratio due to issues with maintaining a stable flame. As a result, a higher fuel-air ratio was needed to stabilize the flame for the 2.4 bar condition.

3.2 Diagnostic setup

Single camera, single laser shot 2D TiRe-LII is performed to analyze soot along the centerline of the burner. Figure 4 shows a schematic of the optical setup used to create the laser sheet. Here, a 10 Hz, 1064 nm laser beam from a flash-lamp pumped Nd:YAG laser (Quanta-Ray PRO-250) is sent through two pairs of cylindrical lenses. One pair of lenses is used to

expand the beam vertically and the other pair of lenses is used to compress the beam horizontally. A pair of knife edges is used to obtain a tophat laser profile, and the sheet is subsequently relay-imaged to the centerline of the burner. This arrangement forms a 26 mm long, 2 mm thick laser sheet with an average fluence of 80 mJ/cm². A Blackfly CMOS camera (BFS-U3-32S4M, 3.45 μ m pixels) is used to measure the beam thickness and profile. Obtaining a perfect tophat laser profile is challenging, as there are spatial and pulse-to-pulse variations in fluence. The inhomogeneities in laser profile can lead to uneven heating of soot particles inside the sampling volume, which can affect particle sizing results. For the laser profile shown in Fig. 4, the difference in the average and peak fluence resulted in a small 0.04 nm (0.2%) difference in estimated particle size.

In this work, TiRe-LII images are captured at 10 MHz using a high-speed camera (Shimadzu HPV-X2, 55 ns exposure, 32 μ m pixels) with 250 \times 400 pixels and zig-zag interlaced frames. A 640 nm band-pass filter (75 nm FWHM) is used in front of the camera to limit the wavelengths used for the LII measurement and to avoid Swan band emissions. Additionally, a 1064 nm blocking bandstop filter is used to avoid reflections of the laser from metallic surfaces of the soot sampler. Multiple objective lenses, including 35 mm (f/1.8), 85 mm (f/1.4), and 100 mm (f/2.8) lens, are used on the camera to change the field of view. A delay generator (Stanford DG645) is also used to synchronize the camera and laser timing. Here, the laser pulse is delayed by 1 μ s after camera acquisition to ensure that the background flame incandescence is captured. Due to download speed limitations, the camera was set to capture a dataset (256 frames) from a single laser shot every 10 s.

In order to thermophoretically extract flame-generated soot, the burner is equipped with a custom designed electro-mechanical soot sampling system [45, 46] similar to that of Vargas and Gülder [47], as shown in Fig. 3b. The soot extraction system is composed of a motor that drives the rotation of the sampling assembly. On each of the ten spokes of the assembly, a single 3.05 mm 400 mesh copper TEM grid is supported. Iterative testing is used to determine the optimal rotational speed needed to gather a sufficient number of soot particles but not damage the grid or cause soot morphology changes. Based on these criteria, a TEM grid residence time of 125 ms is selected. Following the extraction of physical soot samples, the TEM grids are examined with a FEI Tecnai G2-F30 transmission electron microscope. The particle sizes from the TEM data are determined by manually identifying the soot particles on the acquired images with the help of ImageJ software. For this study, the flame generated soot samples are thermophoretically collected at a height of 35 mm from the nozzle tip using the custom designed soot sampler. Soot samples are acquired by rotating the TEM grids through the flame, which is immediately followed by 2D TiRe-LII data acquisition.

4 Results

4.1 Extractive soot sampling

Figure 5 shows some of the larger soot chains present in the TEM images of the extracted soot samples. Figure 5a and b represents canonical soot chains, where primary particles aggregate form branching chain soot structures. Figure 5c depicts the reattachment of the soot chain onto itself, forming closed loop structures, and coalescence of the soot mass fractals, which is an indicator for reactive soot particles. Delimiting the boundaries of the primary soot particles becomes more difficult when soot begins to coalesce. Overall, this behavior is consistent with soot emissions data from a jet stirred reactor [48].

While the vast majority of collected particles are soot aggregates, a small number of other nvPM particles are also present in the flow. These include uniform spherical particles (Fig. 6a) and porous spherical structures with varying contrast (Fig. 6b). While the homogeneous structures are generally due to the presence of Fe/B/Ca/P [49, 50], the porous spherical structures are hypothesized to form in the presence of sulfur [51]. Other non-soot features include the presence of sharp contrasted mineral-like structures, as shown in the boxed portion of Fig. 6b, and fiber-like structures, as shown in Fig. 6c. These are identified to be either carbon nanotubes or goethites [49]. Overall, the presence of non-soot features

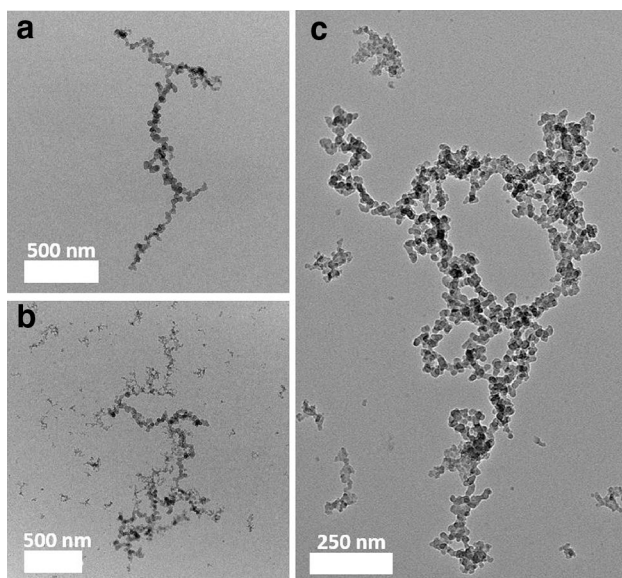


Fig. 5 Examples of typical soot chains are shown including **a** an isolated chain (sampled at 3.8 bar, FAR = 0.16), **b** a large chain with multiple particle sizes (sampled at 2.4 bar, FAR = 0.26) and **c** a large chain with closed ring structures (sampled at 2.4 bar, FAR = 0.26)

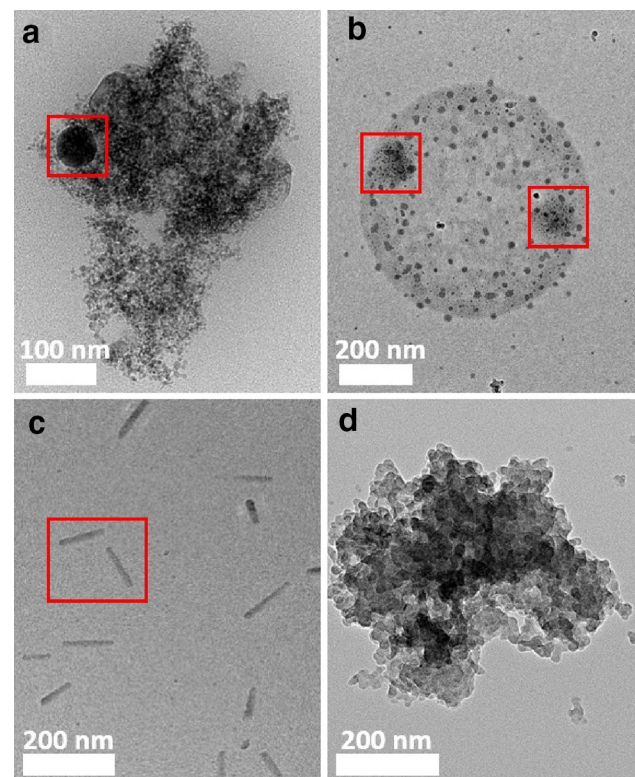


Fig. 6 Other non-volatile particulate matter can also occasionally be found in the flame. Examples include **a** a uniform spherical particle, **b** a porous spherical structure with clusters of sharp contrasted mineral-like structures, **c** fiber-like structures, and **d** a compact aggregate formed due to soot restructuring. All four examples are taken from the 2.4 bar, FAR = 0.26 test point

are likely a result of the complex chemical composition of Jet-A and its additives. Metals are often added to Jet-A to increase combustion temperature, which may result in metal particles in the emissions from Jet-A flames. Finally, Fig. 6d shows compact aggregates formed due to restructuring of soot chains. Baldelli et al. [49] attributed the presence of these compact aggregates to the exposure of the soot aggregates to sulfuric acid [49, 52], which causes them to coalesce. Determination of the exact effects of these non-soot particles and restructured compact aggregates on TiRe-LII particle sizing results require further investigation. However, for the purposes of this study, since these features make up only a small percentage of the data (<5%), the effects are assumed to be negligible.

4.2 2D TiRe-LII

To estimate the primary particle sizes of soot using the LII model, the combustion properties and soot properties must first be determined. One such parameter, the aggregate size, N_p , determines how heat transfer processes occur for primary particles inside an aggregate. In particular, the

aggregate size can be used to account for shielding effects, where particles in an aggregate tend to cool slower compared to isolated primary particles. With shielding, particles are partially or entirely hidden from the soot aggregate exterior and have less surface area for collisions with the ambient gas. Because including a soot aggregate size distribution would introduce several unknown parameters, a simplified method with a constant average aggregate size is used. Using results from TEM images, an estimated average aggregate size of 200 is used for the soot aggregates. This is confirmed by analyzing 30 random aggregates across all test conditions from the TEM images of soot samples, yielding an average aggregate size of 192 with 95% of the aggregates containing between 154 and 229 soot particles. While assuming a constant aggregate size may introduce some uncertainties to the model, a prior study showed that some uncertainty in N_p had negligible effects on the temporal incandescence decay rate when compared with the sensitivity of other parameters [39].

Using this information, the LII model described in Sect. 2 is used to simulate the LII signal decay. Since most soot primary particle sizes are expected to be within the range of 5–60 nm (confirmed through TEM images), these values were used as inputs to the model. The other model parameters are shown in Table 1. Then, simulated decay curves are obtained for each particle size in this range for the three separate pressure conditions. To speed up decay profile fitting, exponential decay curves are first fitted to the model results to create a decay time to particle size relationship. Exponential decay functions do a good job of reproducing the observed incandescence decay profiles when at low laser fluences because heat transfer is dominated by conduction processes at low laser fluences. Thus, exponential decay functions serve as a good intermediary conversion factor. This decay time to particle size relationship is then fit to a polynomial to obtain a library function that outputs an estimated primary particle size for a given input signal decay time constant. By fitting exponential decay curves to the experimental data and using the library conversion function, it is possible to quickly obtain estimated primary particle sizes for every pixel in a 2D image.

Figure 7a shows an example of data collected from the high-speed camera for a single laser shot. Here, the frames

prior to laser incidence can be used for background correction while the frame that occurs immediately after the laser shot serves as the prompt LII signal. Example videos are shown in Supplementary Video 1. To obtain experimental time constants, the intensity is extracted from each frame and backgrounds are removed. Then, an exponential decay time constant is fit to each pixel. A typical 2D image takes approximately 30 to 45 s to fit, varying based on the number of pixels with signal in a dataset. The 2D image of time constants is shown in Fig. 7b. The library function obtained from running the LII model can then be used on each pixel of the time constant image to obtain a 2D image of estimated soot primary particle size, as shown in Fig. 7c. The conversion process using the library function technique is very quick, typically taking less than a second per image.

A visual comparison of the prompt LII image (image taken immediately after the laser pulse arrival) and the time constant image shows that the signal intensities of the two are not heavily correlated, which indicates that regions with a higher volume fraction of soot have similar primary particle sizes to regions with lower volume fractions. From both the time constant and particle size images, slightly larger particles can be seen slightly higher in the flame. This suggests that as soot particles travel up the flame, they mature and form larger aggregates.

Figure 8 shows examples of background-subtracted image intensities for the three pressure conditions in a region of the flame that is at a height of 35 mm above burner. In this figure, the dotted line decay curves are obtained by fitting an exponential decay to the average intensity value in the local region. The standard deviation, shown by the error bars, represents the variation in the intensity in the local region; the standard deviation tends to decrease as the intensity decays to the background level. Results clearly show that increasing the ambient pressure produces faster incandescence signal decay rates due to the increased rate of heat conduction to the surrounding gas.

In order to determine the fitting uncertainty, the R^2 and adjusted R^2 values were measured and tended to be above 0.95 with low sum of squared errors (below 0.01). For the 3.8 bar case in Fig. 8, there was sufficient signal at 0 ns and 100 ns to fit an exponential decay curve resulting in an R^2 value of above 0.97. Alternative fitting parameters were tested, but this did not improve the goodness of fit beyond what is shown in the figure. It is important to note that, with the current diagnostic setup and small soot particle sizes, 3.8 bar is likely close to the maximum pressure at which particle sizing can be reliably conducted in this flame using the 10 MHz sampling rate.

Table 1 LII model input parameters for particle sizing

LII model input parameters	
Aggregate size (N_p)	200
Soot absorption function ($E(m)$)	0.3 [53]
Laser fluence (F_0)	0.08 J/cm ²
Laser wavelength (λ)	1064 nm
Thermal accommodation coefficient (α)	0.43 [54]
Bath gas temperature (T_g)	1800 K

Fig. 7 **a** Time-series LII data is shown with examples illustrated in Supplementary Video 1. **b** The time-series data is fit to produce an image of the time decay constants of soot incandescence. **c** This data is then fit with the LII model to produce 2D estimates of the primary soot particle sizes within the flame

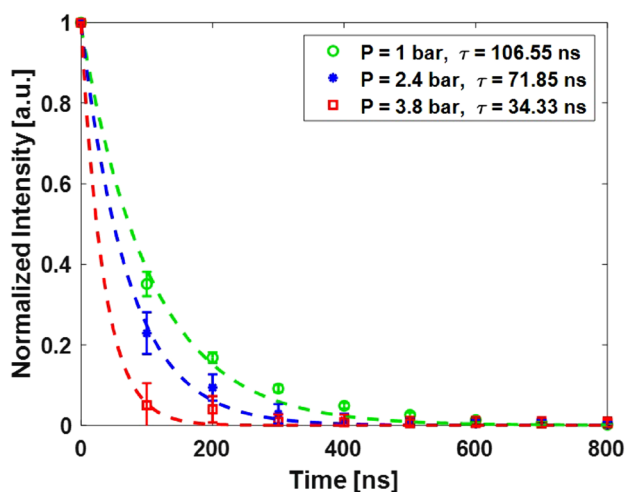
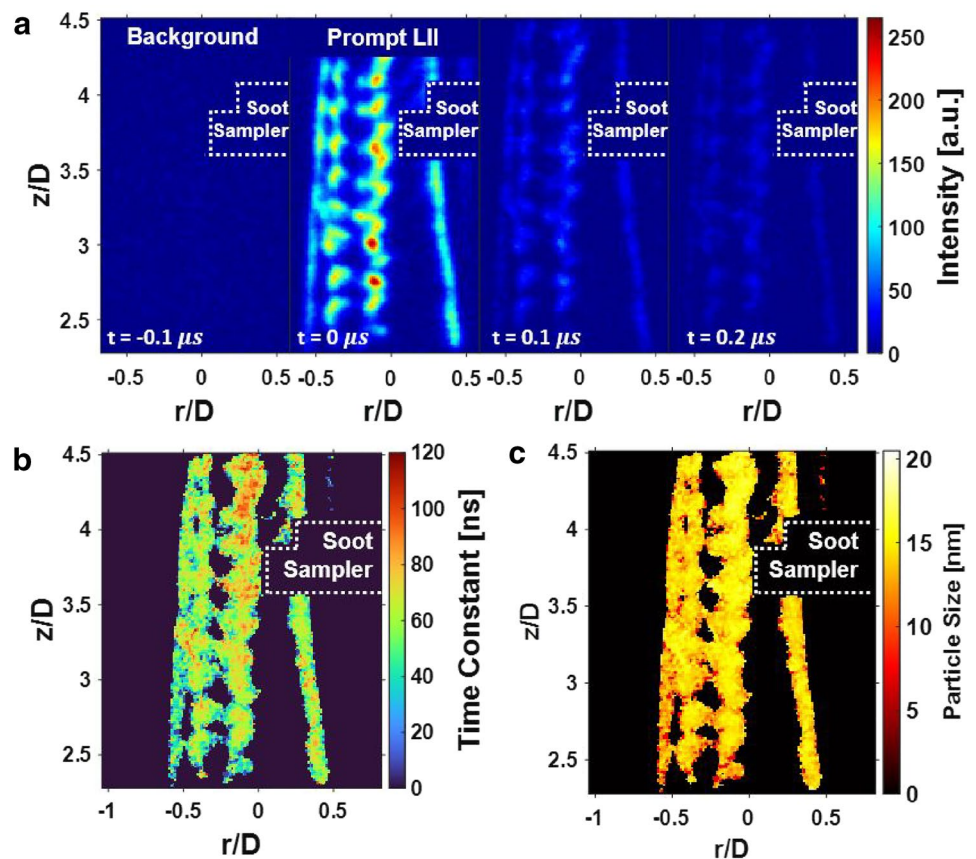


Fig. 8 Incandescence signal decays are shown for 1, 2.4, and 3.8 bar pressure conditions for TiRe-LII data collected at 35 mm height above burner exit. The dots represent experimental data and the dotted lines are the experimental exponential decay fits

4.3 Data comparison

The resulting primary particle size distributions from both the TiRe-LII data and extractive soot samples are shown

in Fig. 9. Error bars in this figure show the standard deviation assuming Poisson statistics for each bin. It should be noted that soot sample data shows individual soot particle sizes collected at 35 mm above the burner while LII data is provided as an estimate of the primary particle size in each pixel over an area of 20 to 40 mm above the burner. Since soot particle sizes are not monodisperse, LII measurements may bias towards larger primary particle sizes due to the longer decay times. For the soot sampling data, 230, 514, and 292 particles are measured for the 1, 2.4, and 3.8 bar conditions, respectively. Particle sizes were extracted from different aggregates in order to be statistically independent. For the TiRe-LII data, 1,290, 10,346, and 56,324 pixels are measured for the 1, 2.4, and 3.8 bar conditions, respectively. Because 2D TiRe-LII is an imaging technique, significantly more samples are obtained from a single laser shot. These data are also relatively quick to process, providing instantaneous soot particle size distributions over a large area.

In the distributions in Fig. 9, the median soot particle diameters are between 13 nm to 16 nm. For all pressure conditions, the median diameters obtained from soot sampling and TiRe-LII are within 2 nm, showing a good match between the TiRe-LII data, LII model, and extractive soot sampling results. Since this experiment utilizes a premixed prevaporized Jet-A flame, smaller particle sizes can be

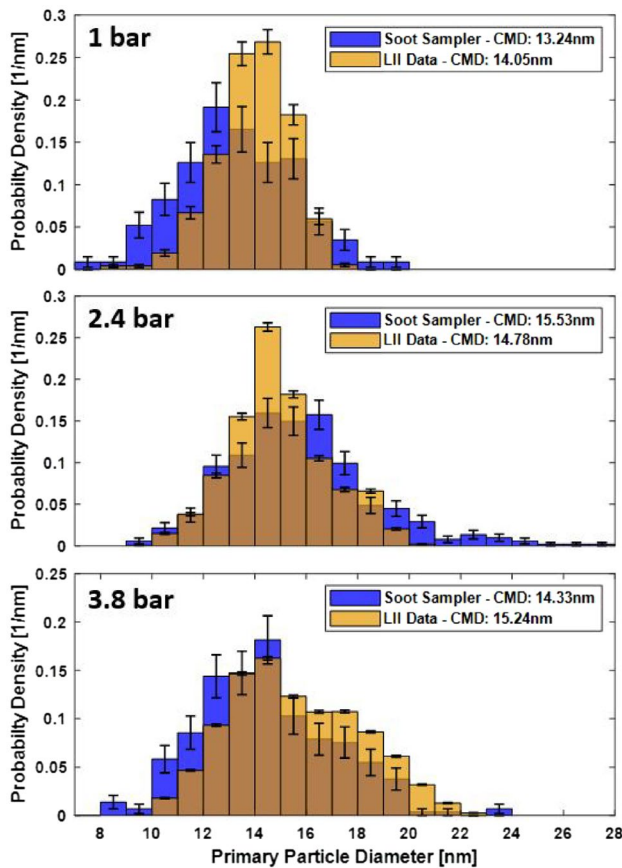


Fig. 9 Particle size distributions for both TiRe-LII and extracted soot samples are shown for 1, 2.4, and 3.8 bar pressure conditions. The count median diameters (CMD) are listed for each distribution. Error bars show the standard deviation of the results

expected as combustion may be more complete with better premixing. The smaller particle sizes are also consistent with values from other studies on soot emissions from aircraft engines and premixed jet fuel flames [55, 56, 57].

4.4 Model parameter sensitivity analysis

To evaluate the reliability of the LII model, it is important to quantify the uncertainties that come from the use of different model parameters for particle size estimation. In this model, some of the most important parameters are the thermal accommodation coefficient $\alpha(T)$, the soot absorption function $E(m)$, the bath gas temperature T_g , and temperature-dependent properties such as the soot density ρ_s . The thermal accommodation coefficient can vary significantly depending on experimental conditions. For example, in a study by Snelling et al. investigating the thermal accommodation coefficient of soot produced in an ethylene flame, the value of the parameter was determined to be $\alpha(T) = 0.37$ [39]. However, another study found the parameter to be different when accounting for the aggregation

properties of soot, where the value was determined to be $\alpha(T) = 0.43$ [54]. While the difference in parameter values between the two studies is 16%, the difference in particle size estimates is only 5.2% for the range of time constants encountered in this study. Since the value of $\alpha(T) = 0.43$ was determined taking aggregation effects into account, it is used in the model for this study as it better represents the experimental conditions encountered in this study. The increase in the value of the thermal accommodation coefficient is also consistent with a study that investigated the value in a diesel spray flame, and found the value to be around 0.47 when accounting for aggregation effects [58].

The soot absorption function $E(m)$, which largely affects the peak temperature reached during the heating stage, also varies with several experimental factors. The study by Snelling et al. found that $E(m) = 0.4$ [39] for experiments conducted with an ethylene flame. For kerosene, Maugendre determined that $E(m)$ is around 0.3 at 1064 nm [53]. Similarly, [59, 60] determined that the value of $E(m)$ for relatively mature soot should be about 0.29 at 1064 nm for diesel. For a difference of 0.1 in $E(m)$, a particle size estimate difference of only 0.02 nm (0.1%) was noted for the time constant range measured in this study. This error, however, does grow with time constant, meaning in experiments where long decay times are encountered, variations in $E(m)$ may introduce more uncertainty. It should be noted that large uncertainties in the value of $E(m)$ can be found in the literature, as many experimental factors can affect the value of the parameter. For this study, since the fuel used was Jet-A, the value of $E(m) = 0.3$ determined in studies using complex fuels is used in the model.

In most flames, there are spatial variations in local bath gas temperature, which may be more severe in turbulent or unsteady cases. For the current model, a 5% change in the bath gas temperature yields a 3.5% change in estimated particle size. Similarly, a study done by Cenker et al. showed about a 10% change in particle size for a 10% change in bath gas temperature [61]. This indicates that for a large spatial variation in bath gas temperature, large errors may be introduced by assuming a constant bath gas temperature.

Another model assumption that is commonly made is to use constant values for soot properties, including soot density [32]. For the data processed in this study, a temperature-dependent density was implemented based on values given by Fried and Howard [34]. The difference in estimated particle size between the constant and temperature-dependent density model ranged from 0.88 nm to 1.1 nm for the range of time constants measured in this study. Thus, assuming constant properties, including constant soot density, may introduce errors into the particle size estimates.

5 Conclusions

In this work, we explore the application of a unique 2D TiRe-LII technique in a Jet-A flame at elevated pressures for the first time. This method is used to estimate soot particle sizes in a 2D plane with a single laser shot and a single camera, making it an efficient method for collecting instantaneous data on soot formation in the flame. To evaluate the accuracy of these soot particle size estimates, TiRe-LII is deployed with nearly-simultaneous extraction of soot samples using a custom sampling system and TEM analysis. The results obtained from extractive soot sampling and TiRe-LII match well, with both methods yielding median particles sizes between 13 nm and 16 nm for a height range of 20 mm to 40 mm above the burner. These small particle sizes are also within expectations for the soot growth region in the flame and are similar to other examples from the literature for Jet-A fuels [55, 56, 57]. Aside from normal soot chains made of primary particles, uniform spherical particles, mineral-like particles, fiber structures, and restructured soot aggregates were also seen in the collected samples. While these particles require further investigation, they make up a very small percentage of the total number of particles and hence have a minimal effect on LII model fitting.

From the model parameter sensitivity analysis, it is clear that $\alpha(T)$ has the greatest impact on the conduction cooling rate and decay rate of the LII signal, and thus the estimates of particle size. $E(m)$ appears to have the greatest impact on the peak temperature reached during the heating stage, but only a small influence on the decay rate of the LII signal for the time constant range measured in this study. Additionally, uncertainties can be introduced into the particle size estimates from assuming a constant bath gas temperature or a constant value for properties such as the soot density. Based on this analysis, it is clear that additional measurements of bath gas temperature and other parameters can help reduce the uncertainties in particle size estimation.

While TEM images of extracted soot samples can provide accurate particle size estimates without the same uncertainties present in LII models, extracting soot samples is intrusive by nature. Moreover, TEM images can be time consuming to acquire and process. Thus, the technique would be difficult to apply in a large number of positions in the flow and would be impossible to apply for obtaining instantaneous profiles of soot particle sizes in unsteady flames. The 2D TiRe-LII technique outlined in this work provides an alternative, non-intrusive method for determining soot particle sizes. In order to obtain accurate particle sizes using this method, typical aggregate sizes must be determined, accurate parameters must be input to the model, and uncertainties must be characterized.

This work is the first to demonstrate using nearly-simultaneous soot extraction and TiRe-LII data collection to evaluate TiRe-LII estimates of soot particle size in a Jet-A flame at elevated pressures. 2D TiRe-LII can be used to collect large quantities of single shot data from a 2D plane inside the flow. This data can also be quickly and efficiently processed using the automated algorithms described here. The 2D TiRe-LII technique is useful not only for obtaining 2D data, but also useful for collecting primary particle size data in environments where extractive soot sampling is cumbersome or infeasible.

The techniques discussed in this work can potentially be used in the future for studying soot production and emissions in high pressure lean prevaporized premixed and rich-quench-lean aeroengine combustors. By interlacing data collection on multiple ultra-high-speed cameras to achieve acquisition at 20 MHz or more, particle sizing at even higher pressures can potentially be achieved. Overall, the time-resolve LII techniques discussed in this work can potentially be used for a variety of application from combustor design to nanomaterial manufacturing to atmospheric science.

Supplementary Information The online version contains supplementary material available at <https://doi.org/10.1007/s00340-023-08015-w>.

Acknowledgements This research was funded by the U.S. Federal Aviation Administration Office of Environment and Energy through ASCENT, the FAA Center of Excellence for Alternative Jet Fuels and the Environment, Project 74 through FAA Award Number 13-C-AJFE-GIT-079 under the supervision of Nicole Didyk-Wells. Any opinions, findings, conclusions or recommendations expressed in this material are those of the authors and do not necessarily reflect the views of the FAA.

Data availability The data generated during and/or analyzed during the current study are available from the corresponding author on reasonable request.

References

1. R.C. Moffet, K.A. Prather, Proc. Natl. Acad. Sci. **106**, 11,872 (2009)
2. J. Hansen, L. Nazarenko, Proc. Natl. Acad. Sci. **101**, 423 (2004)
3. M. Commodo, F. Picca, G. Vitiello, G.D. Falco, P. Minutolo, A. D'Anna, Proc. Combust. Inst. **38**, 1487 (2021)
4. G.C. Borillo, Y.S. Tadano, A.F.L. Godoi, T. Pauliquevis, H. Sarmiento, D. Rempel, C.I. Yamamoto, M.R. Marchi, S. Potgieter-Vermaak, R.H. Godoi, Sci. Total Environ. **644**, 675 (2018)
5. K.M. Bendtsen, E. Bengtsen, A.T. Saber, U. Vogel, Environ. Health **20**, 1 (2021)
6. R.K. Mishra, S. Chandel, Int. J. Turbo Jet Eng. **36**, 61 (2016)
7. M. Maricq, S.J. Harris, J.J. Szente, Combust. Flame **132**, 328 (2003)
8. B. Zhao, Z. Yang, M.V. Johnston, H. Wang, A.S. Wexler, M. Balthasar, M. Kraft, Combust. Flame **133**, 173 (2003)
9. H. Michelsen, C. Schulz, G. Smallwood, S. Will, Prog. Energy Combust. Sci. **51**, 2 (2015)

10. Z. Zhang, L. Zhou, X. He, *Appl. Energy Combust Sci.* **13**, 100,103 (2023)
11. T.A. Sipkens, J. Menser, T. Dreier, C. Schulz, G.J. Smallwood, K.J. Daun, Laser-induced incandescence for non-soot nanoparticles: recent trends and current challenges. <https://doi.org/10.1007/s00340-022-07769-z>, *Appl. Phys. B* **128**, 72 (2022)
12. Y. Chen, E. Cenker, D.R. Richardson, S.P. Kearney, B.R. Halls, S.A. Skeen, C.R. Shaddix, D.R. Guildenbecher, *Opt. Lett.* **43**, 5363 (2018)
13. F. Liu, M. Yang, F.A. Hill, D.R. Snelling, G.J. Smallwood, *Appl. Phys. B* **83**, 383 (2006)
14. E. Weingartner, H. Burtscher, U. Baltensperger, *Atmos. Environ.* **31**, 2311 (1997)
15. R. Hadeif, K.P. Geigle, W. Meier, M. Aigner, *Int. J. Therm. Sci.* **49**, 1457 (2010)
16. R. Stirn, T.G. Baquet, S. Kanjarkar, W. Meier, K.P. Geigle, H.H. Grotheer, C. Wahl, M. Aigner, *Combust. Sci. Technol.* **181**, 329 (2009)
17. Y. Zhang, F. Liu, D. Clavel, G.J. Smallwood, C. Lou, *Energy* **177**, 421 (2019)
18. G.B. Kim, S.W. Cho, J.H. Lee, D.S. Jeong, Y.J. Chang, C.H. Jeon, *Trans. Korean Soc. Mech. Eng.* **30**, 973 (2006)
19. H. Bladh, J. Johnsson, N.E. Olofsson, A. Bohlin, P.E. Bengtsson, *Proc. Combust. Inst.* **33**, 641 (2011)
20. R.L.V. Wal, T.M. Ticich, A.B. Stephens, *Combust. Flame* **116**, 291 (1999)
21. M. Hofmann, B. Kock, T. Dreier, H. Jander, C. Schulz, *Appl. Phys. B* **90**, 629 (2007)
22. M. Hofmann, W.G. Bessler, C. Schulz, H. Jander, *Appl. Opt.* **42**, 2052 (2003)
23. J.E. Dec, A.O. Zur Loye, D.L. Siebers, *SAE Tech. Pap.* **100**, 277 (1991)
24. G. Wiltafsky, W. Stolz, J. Köhler, C. Espey, The Quantification of Laser-Induced Incandescence (LII) for Planar Time Resolved Measurements of the Soot Volume Fraction in a Combusting Diesel Jet. *SAE Tech. Pap.*, 105, 978–988 (1996). <http://www.jstor.org/stable/44729111>
25. K. Inagaki, S. Takasu, K. Nakakita, In-cylinder Quantitative Soot Concentration Measurement By Laser-Induced Incandescence. *SAE Tech.*, 108, 574–586. (1999). <http://www.jstor.org/stable/44743394>
26. R. Ryser, T. Gerber, T. Dreier, *Combust. Flame* **156**, 120 (2009)
27. K.P. Geigle, J. Zerbs, R. Hadeif, C. Guin, *Appl. Phys. B* **125**, 96 (2019)
28. M.L. Passarelli, S.E. Wonfor, A.X. Zheng, S.R. Manikandan, Y. Mazumdar, J.M. Seitzman, A.M. Steinberg, H. Bower, J. Hong, K. Venkatesan, M. Benjamin, AIAA Science and Technology Forum and Exposition, AIAA SciTech Forum (2022)
29. H. Michelsen, F. Liu, B. Kock, H. Bladh, A. Boiarciuc, M. Charwath, T. Dreier, R. Hadeif, M. Hofmann, J. Reimann, S. Will, P.E. Bengtsson, H. Bockhorn, F. Foucher, K.P. Geigle, C. Mounaïm-Rousselle, C. Schulz, R. Stirn, B. Tribalet, R. Suntz, *Appl. Phys. B* **87**, 503 (2007)
30. C. Schulz, B. Kock, M. Hofmann, H. Michelsen, S. Will, B. Bougie, R. Suntz, G. Smallwood, *Appl. Phys. B* **83**, 333 (2006)
31. H.A. Michelsen, M.A. Linne, B.F. Kock, M. Hofmann, B. Tribalet, C. Schulz, *Appl. Phys. B* **93**, 645 (2008)
32. F. Liu, G.J. Smallwood, D.R. Snelling, *J. Quant. Spectrosc. Radiat. Transf.* **93**, 301 (2005)
33. M.W. Chase Jr, *J. Phys. Chem. Ref. Data Monogr.* **9** **14**, 535 (1998)
34. L.E. Fried, W.M. Howard, *Phys. Rev. B* **61**, 8734 (2000)
35. A. Filippov, D. Rosner, *Int. J. Heat Mass Transf.* **43**, 127 (2000)
36. N.A. Fuchs, *Pure Appl. Geophys.* **56**, 185 (1963)
37. N.A. Fuchs, R.E. Daisley, M. Fuchs, C.N. Davies, M.E. Straumanis, *Phys. Today* **18**, 73 (1965)
38. P. Wright, *Discuss. Faraday Soc.* **30**, 100 (1960)
39. D.R. Snelling, F. Liu, G.J. Smallwood, O.L. Gülder, *Combust. Flame* **136**, 180 (2004)
40. A. Brasil, T. Farias, M. Carvalho, *J. Aerosol Sci.* **30**, 1379 (1999)
41. S.R. Forrest, T.A. Witten Jr., *J. Phys. A: Math. Theor.* **12**, L109 (1979)
42. A.M. Brasil, T.L. Farias, M.G. Carvalho, *Aerosol Sci. Technol.* **33**, 440 (2000)
43. F. Liu, K. Daun, D. Snelling, G. Smallwood, *Appl. Phys. B* **83**, 355 (2006)
44. B. McCoy, C. Cha, *Chem. Eng. Sci.* **29**, 381 (1974)
45. A. X. Zheng, S. Manikandan, S. E. Wonfor, A. M. Steinberg, & Y. C. Mazumdar, Planar Time-Resolved Laser-Induced Incandescence for Particulate Emissions in Premixed Flames at Elevated Pressures. In AIAA SCITECH 2023 Forum (p. 2435) (2023)
46. S.R. Manikandan, Characterization of non-volatile particulate matter in pressurized laminar jet-a flames via thermophoretic sampling. Master's thesis (2022)
47. A.M. Vargas, O.L. Gülder, *Rev. Sci. Instrum.* **87**, 055,101 (2016)
48. X. Hu, Z. Yu, L. Chen, Y. Huang, C. Zhang, F. Salehi, R. Chen, R.M. Harrison, J. Xu, *Combust. Flame* **236**, 111,760 (2022)
49. A. Baldelli, U. Trivanovic, J.C. Corbin, P. Lobo, S. Gagné, J.W. Miller, P. Kirchen, S. Rogak, *Aerosol Air. Qual. Res.* **20**, 730 (2020)
50. J. Xing, L. Shao, W. Zhang, J. Peng, W. Wang, C. Hou, S. Shuai, M. Hu, D. Zhang, *J. Environ. Sci.* **76**, 339 (2019)
51. W. Li, L. Shao, D. Zhang, C.U. Ro, M. Hu, X. Bi, H. Geng, A. Matsuki, H. Niu, J. Chen, *J. Clean. Prod.* **112**, 1330 (2016)
52. J. Pagels, A.F. Khalizov, P.H. McMurry, R.Y. Zhang, *Aerosol Sci. Technol.* **43**, 629 (2009)
53. M. Maugendre, Study of soots particles in kerosene and biofuel flames. Ph.D. thesis (2009)
54. S.A. Kuhlmann, J. Reimann, S. Will, *J. Aerosol Sci.* **37**, 1696 (2006)
55. A. Liati, D. Schreiber, P. Alpert, Y. Liao, B. Brem, P.C. Arroyo, J. Hu, H. Jonsdottir, M. Ammann, P.D. Eggenchwiler, *Environ. Pollut.* **247**, 658 (2019)
56. W. Liu, X. Liang, A. Li, B. Lin, H. Lin, D. Han, *Fuel* **267**, 117,244 (2020)
57. A. Liati, B.T. Brem, L. Durdina, M. Vögtli, Y.A.R. Dasilva, P.D. Eggenchwiler, J. Wang, *Environ. Sci. Technol.* **48**, 10,975 (2014)
58. S. Menanteau, R. Lemaire, *Entropy* **22**, 21 (2019)
59. J. Yon, R. Lemaire, E. Therssen, P. Desgroux, A. Coppalle, K.F. Ren, *Appl. Phys. B* **104**, 253 (2011)
60. R. Lemaire, S. Menanteau, Modeling laser-induced incandescence of Diesel soot—Implementation of an advanced parameterization procedure applied to a refined LII model accounting for shielding effect and multiple scattering within aggregates for $\alpha_{-T} \alpha_{+T}$ and $E_{left} E_{m}$ assessment. *Appl. Phys. B* **127** 1–19 (2021)
61. E. Cenker, G. Bruneaux, T. Dreier, C. Schulz, *Appl. Phys. B* **119**, 745 (2015)

Springer Nature or its licensor (e.g. a society or other partner) holds exclusive rights to this article under a publishing agreement with the author(s) or other rightsholder(s); author self-archiving of the accepted manuscript version of this article is solely governed by the terms of such publishing agreement and applicable law.